

# Superelastic Graphene-Based Composite Aerogel for Thermal and Electromagnetic Protection in Extreme Temperature Environments

Junwei Yue, Mengmeng Qin,\* Huitao Yu, Qingxia He, and Wei Feng\*

The aerogel materials stacked with nanomaterials usually have good thermal insulation and electromagnetic wave (EMW) absorption properties due to their porous properties. However, consecutive mechanical loading cycles under extreme temperature environments cause irreversible structural and mechanical damage. Furthermore, there is an inherent contradiction between the characteristics of multiple interfaces and their anti-fatigue performance. In this study, polyimide (PI) fibers are dispersed in graphene aerogel, and the composite aerogel (G-PI@F<sub>20</sub>/CNT<sub>x</sub>) can be formed by in situ welding. The hierarchical porous structure endows aerogel with excellent superelasticity, thermal insulation, and EMW absorption properties. The aerogel endures 90% strain compression cycles over a temperature range of  $-196$  to  $160$  °C, with deformation loss remaining below 5%. This hierarchical porous structure hinders phonon conduction, resulting in low thermal conductivity ( $0.0313 \text{ W m}^{-1} \text{ K}^{-1}$ ). The aerogel with a thickness of 4.1 mm achieves an effective absorption bandwidth (EAB) of 12.48 GHz. By increasing the thickness to 20.3 mm, ultra-broadband absorption of 15.24 GHz and an optimal reflection loss (RL<sub>min</sub>) of  $-43.49$  dB are attained. These findings provide crucial insights into the design of multifunctional EMW absorbing materials and offer a general strategy for synthesizing superelastic aerogels.

In recent years, extensive research has been conducted to develop innovative EMW absorbing materials with enhanced absorption capacity, broadband absorption, reduced thickness, and lightweight characteristics.<sup>[6–11]</sup> While significant advancements have been made in improving EMW absorption performance, the effective application of these materials under extreme temperature conditions remains a major challenge, necessitating further improvements in their overall properties.<sup>[12,13]</sup>

Electromagnetic protection under extreme temperature conditions requires materials with superior thermal insulation properties and mechanical robustness to endure severe temperature fluctuations and complex external stresses.<sup>[13–15]</sup> To meet the requirements for electromagnetic and thermal protection in extreme environments, extensive research has been conducted. For instance, Li et al.<sup>[16]</sup> developed an ultra-flexible boron nitride nanoribbon aerogel capable of withstanding 80% strain in liquid nitrogen without fracturing. This aerogel also retains exceptional compressive,

bending, and twisting elasticity across a wide temperature range, from liquid nitrogen temperatures to above  $1000$  °C. Similarly, Zhang et al.<sup>[17]</sup> introduced a ceramic nanofiber aerogel exhibiting ultra-elasticity under 90% strain, along with high-temperature resistance and thermal insulation performance up to  $1300$  °C. Although aerogels offer outstanding mechanical and thermal insulation properties, conventional insulating ceramic materials generally lack effective EMW absorption capability. Cai et al.<sup>[18]</sup> fabricated Si<sub>3</sub>N<sub>4</sub>/SiC aerogels with favorable dielectric properties, achieving an effective absorption bandwidth (EAB) of 8.62 GHz and an optimal reflection loss (RL<sub>min</sub>) of  $-52.31$  dB. These aerogels also demonstrated excellent thermal shock resistance ( $-196$  to  $900$  °C) and thermal insulation properties while preserving structural integrity under 50% strain during compression cycling at room temperature. However, maintaining both structural stability and performance under large deformation (90%) compression cycling in ultralow-temperature environments remains a considerable challenge, especially for nanocomposite aerogels with a large number of interfaces.

In the aerospace sector, extreme temperature variations, limited space availability, and high multifunctionality demands

## 1. Introduction

With the continuous advancement of wireless communication and radar detection technologies, the utilization of electromagnetic wave (EMW) has become widespread across various fields, particularly in the military, aerospace, and communication sectors.<sup>[1,2]</sup> EMW absorbing materials serve a critical function in shielding the human body from electromagnetic radiation, protecting electronic devices from electromagnetic interference, and improving the radar stealth capabilities of military equipment.<sup>[3–5]</sup> Consequently, the demand for high-performance EMW absorbing materials has grown increasingly pressing.

J. Yue, M. Qin, H. Yu, Q. He, W. Feng  
School of Materials Science and Engineering and Tianjin Key Laboratory of Composite and Functional Materials  
Tianjin University  
Tianjin 300072, P. R. China  
E-mail: qmm@tju.edu.cn; weifeng@tju.edu.cn

The ORCID identification number(s) for the author(s) of this article can be found under <https://doi.org/10.1002/adfm.202508319>

DOI: 10.1002/adfm.202508319

impose significant challenges on the application of EMW-absorbing materials. Consequently, the development of ultralow-density multifunctional EMW absorbing materials that combine superior absorption, thermal insulation, and mechanical properties while maintaining stability under extreme temperature fluctuations has become a crucial issue requiring urgent attention. Although various studies have been conducted, certain limitations persist. For instance, Gu et al.<sup>[19]</sup> designed a leaf-vein-structured MXene/CNTs/PI aerogel that demonstrated compressive elasticity and structural stability under 50% strain across a broad temperature range of  $-196$  to  $400$  °C. This material achieved an  $RL_{\min}$  of  $-75.8$  dB and an EAB of  $7.14$  GHz. However, its compressibility is restricted to 50% across this temperature range, leading to considerable space occupation in practical applications, and its EAB remains relatively narrow. Similarly, Wang et al.<sup>[20]</sup> developed a carbon-based aerogel (FCS) with adjustable compressive strain ranging from 0% to 75%, enabling modulation of the EAB to  $13.4$  GHz while exhibiting excellent thermal insulation performance. Although broadband absorption was achieved through compression regulation, the FCS material necessitates thickness adjustments to align with incident waves under electromagnetic interference, making it challenging to maintain optimal EMW absorption performance and stable thermal insulation simultaneously.

Herein, a graphene-based composite aerogel (G-PI@F<sub>20</sub>/CNT<sub>x</sub>) was designed as an EMW absorbing material to address the challenges associated with simultaneously optimizing large-strain superelasticity, extreme-temperature thermal protection, and EMW absorption properties. The G-PI@F<sub>20</sub>/CNT<sub>x</sub> incorporates a distinctive 3D polyimide (PI) fiber “welded” skeleton and a hierarchical porous structure, where leaf-vein-like interconnected pore walls establish an integrated network that effectively minimizes pore wall slippage and structural collapse. As a result, the aerogel maintains superelasticity under large-strain compression, even within a temperature range of  $-196$  to  $160$  °C. Furthermore, the aerogel exhibits vacuum compressibility and bending elasticity, achieving a volume difference of up to 90% between its compressed and expanded states. Due to its high porosity, the aerogel demonstrates superior thermal insulation, with a thermal conductivity as low as  $0.0313 \text{ W m}^{-1} \text{ K}^{-1}$ . The unique hierarchical porous structure within the aerogel effectively prolongs the transmission path of EMW and provides multiple reflection spaces. In combination with excellent impedance matching and an electromagnetic synergy loss mechanism, the aerogel exhibits remarkable EMW absorption properties. With a thickness of  $4.1$  mm, the aerogel achieves a broadband effective absorption of  $12.48$  GHz ( $5.52$ – $18$  GHz). When the thickness is increased to  $20.3$  mm, the  $RL_{\min}$  and EAB reach  $-43.49$  dB and  $15.24$  GHz ( $2.76$ – $18$  GHz), respectively, indicating ultra-broadband absorption properties. Radar cross-section (RCS) simulations and application scenario verifications further confirm the aerogel’s outstanding comprehensive performance. As a multifunctional EMW absorbing material, G-PI@F<sub>20</sub>/CNT<sub>x</sub>, which exhibits large-strain superelasticity, flame retardancy, extreme-temperature thermal protection, and excellent EMW absorption characteristics, demonstrates significant application potential in the aerospace sector.

**Table 1.** Serial numbers of samples with different CNTs contents and different reduction temperatures.

Sample temperature	G-PI@F <sub>20</sub> /CNT <sub>2</sub>	G-PI@F <sub>20</sub> /CNT <sub>4</sub>	G-PI@F <sub>20</sub> /CNT <sub>6</sub>
$400$ °C	A1	A2	A3
$500$ °C	B1	B2	B3
$500$ °C (1000 compression cycles)	C1	C2	C3
$600$ °C	D1	D2	D3

Note: G stands for reduced graphene oxide. PI stands for polyimide fiber. F stands for Fe<sub>3</sub>O<sub>4</sub> nanoparticles. CNT stands for multi-walled carbon nanotubes.

## 2. Results and Discussion

To address the critical challenges associated with the simultaneous optimization of large-strain superelasticity, extreme-temperature thermal protection, and EMW absorption performance, the G-PI@F<sub>20</sub>/CNT<sub>x</sub> was designed with the objective of achieving: 1) a hierarchical porous structure that facilitates multiple reflections and scattering of EMW while enhancing resistance to extreme thermal shocks; 2) an optimized balance between the attenuation constant and impedance matching; and 3) a highly stable 3D supporting skeleton that maintains compressive elasticity under large deformations. PI fibers possess superior mechanical properties, thermal stability, and a low dielectric constant, while the dielectric constant of graphene oxide (GO) can be precisely tuned over a broad range. This characteristic enables effective modulation of both the elasticity and dielectric properties of the aerogel. A specific ratio of GO and PI fibers ensures the continuity and structural integrity of the aerogel’s pore wall network, while the addition of carbon nanotubes (CNTs) and Fe<sub>3</sub>O<sub>4</sub> nanoparticles further enhances the electromagnetic synergistic mechanism. The 3D electromagnetic loss network, composed of 0D Fe<sub>3</sub>O<sub>4</sub> nanoparticles, 1D CNTs, and 2D graphene, enables multidimensional energy dissipation and enhances the broadband response of the composite.<sup>[21,22]</sup> The serial numbers of G-PI@F<sub>20</sub>/CNT<sub>x</sub> samples treated under various conditions are presented in Table 1 in the experimental section.

### 2.1. Microscopic Structure and Superelastic Mechanism of G-PI@F<sub>20</sub>/CNT<sub>x</sub>

The preparation process of the G-PI@F<sub>20</sub>/CNT<sub>x</sub> involves simple hydrothermal and thermal reduction methods (Figure S1, Supporting Information). PI fibers and CNT were modified to improve the dispersibility (Figure S2, Supporting Information).<sup>[23]</sup> During the hydrothermal reaction, enhanced interfacial interactions among different components promote their self-assembly into a stable 3D structure.<sup>[24,25]</sup> SEM characterization of the aerogel’s internal microstructure (Figure 1a) reveals a distinctive hierarchical porous architecture with numerous small pores between multilayer pore walls (Figure 1a1,a2). This structure originates from the self-assembly process, where the abundant oxygen-containing groups on GO interact with amino or carboxyl groups on PI fibers via hydrogen or ionic bonding.<sup>[26,27]</sup> As a result, the lamellar GO stacks along the PI fiber network in a layered manner, while the guiding and isolating effects of PI fibers facilitate the formation of a stable network, maintaining the

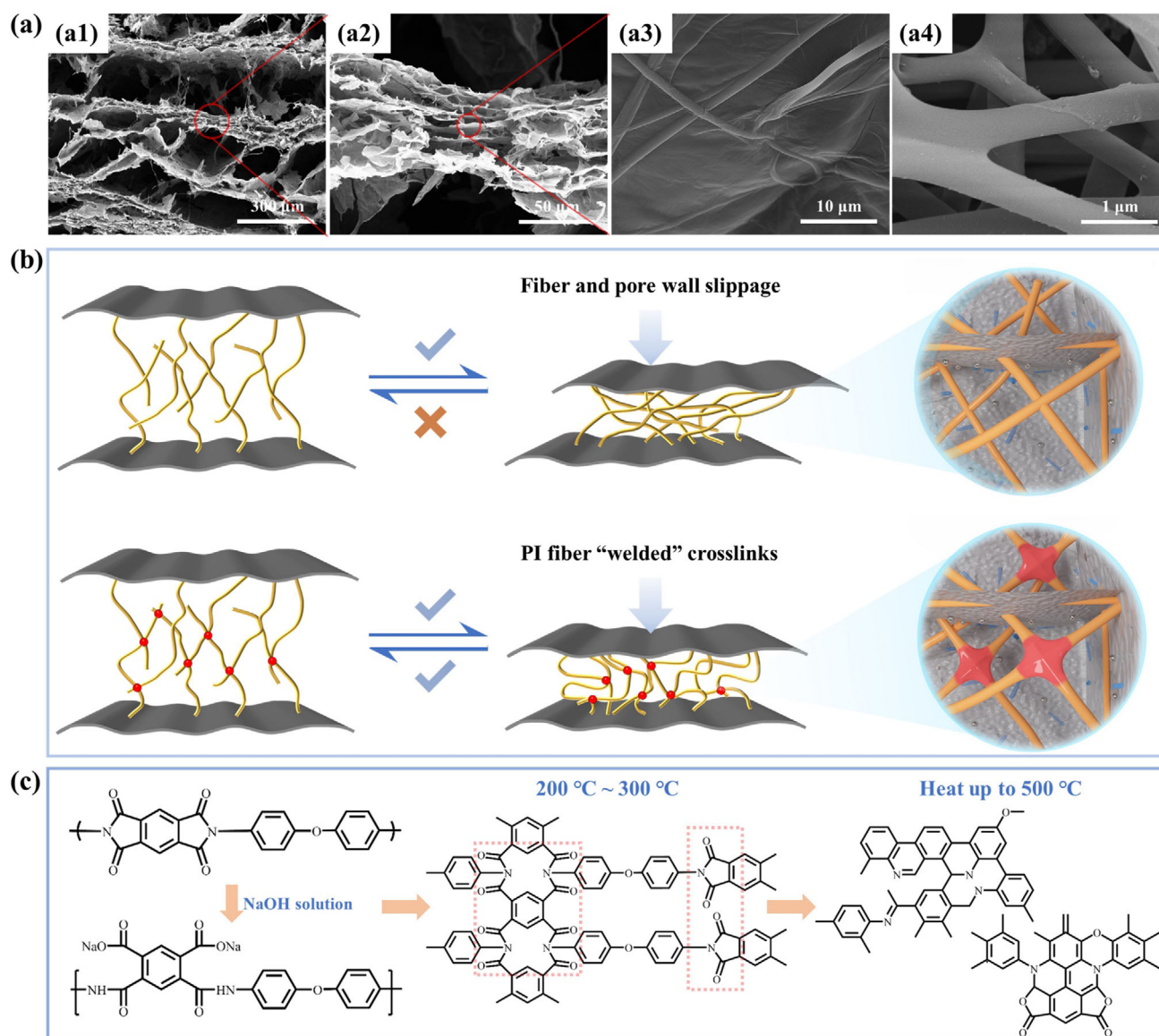


**Figure 1.** a) SEM image of the cross-section of G-PI@F<sub>20</sub>/CNT<sub>4</sub> and the “weld points” in cross-linked PI fiber networks. b) Schematic diagram of the resilience enhancement mechanism of cross-linked PI fiber network. c) Intermolecular and intramolecular thermal imidization reactions and other cross-linking reactions of PI fibers.

multilayered characteristics of the pore wall. BET analysis revealed typical type-IV isotherms, confirming the presence of a mesoporous structure within the aerogel (Figure S3, Supporting Information), with a specific surface area of 58.1787 m<sup>2</sup> g<sup>-1</sup>. This hierarchical porous structure could effectively trap incident EMW like a “cage” inducing multiple reflections and ultimately dissipating them. PI fibers interconnect the pore walls in a vein-like manner, forming a continuous pathway (Figure 1a3), while CNTs and Fe<sub>3</sub>O<sub>4</sub> nanoparticles are uniformly distributed and embedded within the pore walls (Figure S4, Supporting Information). EDS mapping of the aerogel cross-section (Figure S5, Supporting Information) further verifies the homogeneous dispersion of Fe<sub>3</sub>O<sub>4</sub> nanoparticles, which form independently dispersed magnetic loss sites throughout the aerogel.

During large strain compression, conventional graphene-based aerogels irreversibly deform due to pore wall slip/rearrangement and pore structure collapse/deformation.<sup>[28,29]</sup> Incorporating fiber reinforcement into graphene aerogels can effectively enhance their compressive resilience. However, under large strain, the physical entanglement between fibers is not sufficiently robust, and relative slip still occurs. In contrast, G-PI@F<sub>20</sub>/CNT<sub>x</sub> utilizes a crosslinked PI fiber network as the skeleton, which constrains the relative slippage of pore walls and provides structural support to maintain pore stability (Figure 1b). During thermal reduction, PI fibers undergo a crosslinking reaction (Figure 1c). Specifically, alkali-treated PI fibers experience partial imide ring opening, forming corresponding sodium salts.<sup>[30,31]</sup> As thermal reduction progresses,



the high-temperature environment provides sufficient energy to overcome the energy barrier for the cross-linking reactions of PI molecular chains. Consequently, intermolecular and intramolecular thermal imidization, along with other cross-linking reactions, occur on the surface of the entangled PI fibers,<sup>[32]</sup> forming “weld points” at fiber junctions (Figure 1a4). These “weld points” integrate the PI fiber network into a cohesive structure, which is crucial for the aerogel’s superelasticity. Additionally, as the thermal reduction temperature increases, the amide ring on the surface of PI fibers gradually breaks along the C–N and C–O bonds, accompanied by significant dehydrogenation and deoxygenation polycondensation reactions that release CO, CO<sub>2</sub>, and H<sub>2</sub>. At fiber junctions, partial molecular restructuring forms continuous and large aromatic heterocyclic polycyclic compounds. The increased density of cross-linking points further reinforces the fiber network, while hexagonal carbon layers resembling a graphitic structure begin to emerge on fiber surfaces.<sup>[33]</sup> TEM and EDS mapping analyses of thermally treated PI fiber cross-sections (Figure S6, Supporting Information) confirm the presence of a thin carbonized layer on the fiber surface.<sup>[34]</sup> The cross-linked PI fiber network provides robust structural support for the aerogel, and the carbonized layer enhances induced current conduction, thereby improving EMW dissipation.

To investigate the crosslinking mechanism involved in the formation of “weld points,” XPS analysis was conducted to examine the molecular structure evolution of pure PI aerogels before and after thermal treatment at 500 °C (Figure 2a,d). The significant decrease of Na signal intensity indicates the imidization of hydrolyzed PI molecules, causing the detachment of Na ions from carboxyl groups. For untreated PI fibers, the C 1s spectrum can be deconvoluted into four main peaks (Figure 2b) at 284.8 eV (–C–C), 286.0 eV (–C–N–), 288.4 eV (–C=O/–CONH–), and 290.8 eV (–COO–). The N 1s spectrum (Figure 2c) consists of two primary peaks at 398.7 eV (–NH–) and 400.4 eV (–C–N–), confirming that the alkali-treated PI fibers underwent hydrolysis, resulting in partial imide ring opening.<sup>[26,35]</sup> After thermal treatment at 500 °C, the C 1s spectrum (Figure 2e) exhibits four main peaks at 284.8 eV (–C–C), 285.7 eV (–C–N–), 288.1 eV (–C=O/–CONH–), and 290.6 eV (–COO–). The N 1s spectrum (Figure 2f) displays two primary peaks at 399.8 eV (NR<sub>3</sub>, oxygen-containing cyclic structures) and 400.4 eV (–C–N–).<sup>[36]</sup> Under high-temperature conditions, the chemical structure on the fiber surface undergoes rearrangement, with functional groups decomposing or transforming, altering the chemical environment of the elements, and leading to a reduction in binding energy. The comparative analysis of the C 1s and N 1s spectra before and after thermal treatment confirms the occurrence of thermal imidization and crosslinking reactions. Specifically, after thermal treatment, the C 1s spectrum exhibits an enhanced –C–N– peak, a reduced –C=O/–CONH– peak, and an increased –COO– peak within the aromatic ring.<sup>[36,37]</sup> Meanwhile, the N 1s spectrum shows the disappearance of the –NH– peak and intensified NR<sub>3</sub> signal in the aromatic ring. Comparison with the XPS spectra of original PI fibers (Figure S7, Supporting Information) further supports the occurrence of hydrolysis and crosslinking reactions. Additionally, ATR-FTIR analysis (Figure S8, Supporting Information) shows distinct PI characteristic peaks in both original and alkali-treated fibers. The slight reduction in

peak intensity after alkali treatment indicates partial hydrolysis. In contrast, the substantial attenuation of characteristic peaks after heat treatment is attributed to molecular rearrangement on the fiber surface, forming continuous, large aromatic heterocyclic polycyclic compounds.<sup>[36]</sup> These transformations facilitate the in situ welding of PI fibers within the graphene aerogel network.

The hierarchical porous structure and cross-linked PI fiber network endow the G-PI@F<sub>20</sub>/CNT<sub>x</sub> with outstanding compressive resilience. To assess its superelasticity and fatigue resistance, cyclic compression tests were conducted using a universal testing machine and a high–low-temperature test chamber under ultralow (–130 °C), room, and high-temperature (150 °C) conditions. Initially, an ultralow temperature test was conducted using a customized concentric ring mold, with liquid nitrogen injected into the outer cavity to maintain the inner cavity temperature below –130 °C. Under these conditions, aerogel samples underwent 100 compression cycles at 90% strain (Figure 2g). After 50 and 100 cycles, the maximum compressive stress was 13.48 and 13.23 kPa, respectively, retaining 91.02% and 89.33% of the initial stress. The deformation loss after 100 cycles was 4.04%. At room temperature (26 °C), aerogel samples underwent 1000 compression cycles at 90% strain. As shown in Figure 2h, 75.04% and 73.11% of the original maximum stress were retained after 500 and 1000 cycles, respectively. The stress reduction was minimal after 500 cycles, and the total deformation loss after 1000 cycles was 3.62%. Additionally, aerogel samples were tested in a high-temperature environment at 150 °C for 100 compression cycles at 90% strain. As illustrated in Figure 2i, the maximum compressive stress after 100 cycles was 55.31 kPa, retaining 85.62% of the initial value, with a deformation loss of 4.33%. These results indicate that the cross-linked PI fiber network and leaf-vein-like continuous pore wall structure contribute to the aerogel’s outstanding compressive resilience and fatigue resistance (Table S1, Supporting Information). The aerogel retained its elasticity under ultralow, room, and high-temperature conditions, with a shape retention rate exceeding 95% after 100 cycles of 90% strain compression. This exceptional fatigue resistance demonstrates significant potential for practical applications.

To further evaluate the superelasticity of G-PI@F<sub>20</sub>/CNT<sub>x</sub> under extremely low temperatures, the aerogel sample was immersed in liquid nitrogen for 20 min. Subsequently, cyclic compression tests were performed in the liquid nitrogen environment (Movie S1, Supporting Information). The aerogel exhibited negligible deformation loss, confirming its ability to retain superelasticity even at extremely low temperatures (Figure 2j). In addition to external compressive forces, extreme compression was also achieved through vacuuming. The aerogel’s initial volume of ≈12.37 cm<sup>3</sup> was reduced to ≈1.17 cm<sup>3</sup> after vacuum compression, corresponding to a volume compression rate exceeding 90% (Figure 2k). Under both vacuum and non-vacuum conditions, the aerogel withstood complex bending without structural damage and nearly fully recovered upon release (Movies S2 and S3, Supporting Information). The aerogel’s vacuum compression and bending capabilities are essential for space-saving applications. In space environments, solar panels, typically have large surface areas, posing challenges for stealth design. Utilizing the aerogel’s compressive properties, a polyimide film

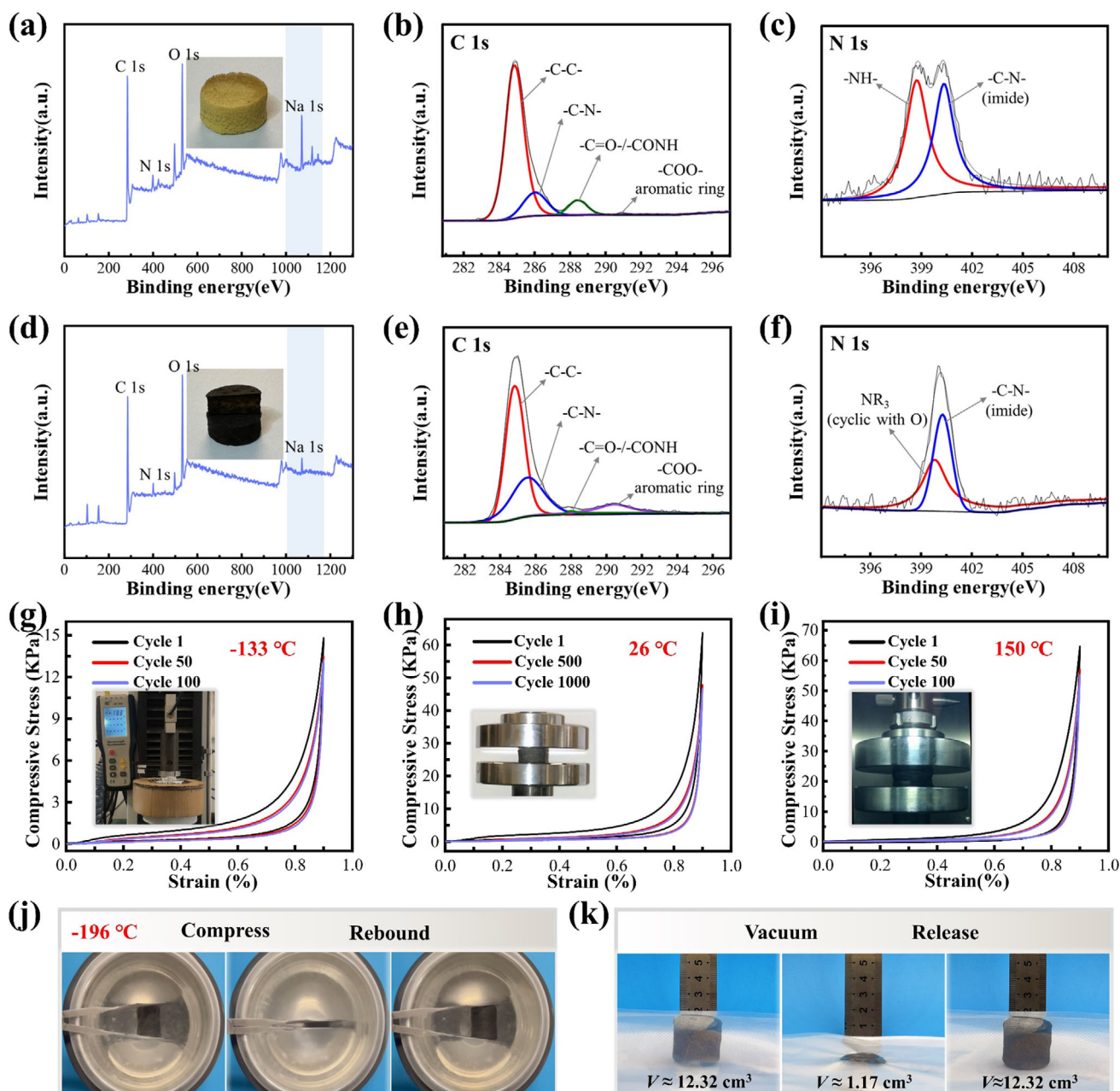


**Figure 2.** XPS spectra of PI fiber aerogel a–c) before and d–f) after thermal treatment at 500 °C. Compression cycle curves of G-PI@F<sub>20</sub>/CNT<sub>4</sub> at g) ultralow temperature, h) room temperature, and i) high temperature. j) Compression cycling process of the aerogel in liquid nitrogen. k) Vacuum compression cycling process of the aerogel.

was coated onto its surface and attached to a folding panel to demonstrate the unfolding and folding process of a solar panel (Movie S4, Supporting Information), presenting a novel strategy for the stealth design of solar panels. Validation tests demonstrated that G-PI@F<sub>20</sub>/CNT<sub>x</sub> exhibits exceptional superelasticity and fatigue resistance under extreme temperature conditions. This superior performance is attributed to the strong structural support from the cross-linked PI network and hierarchical porous architecture, which consists of corrugated pores and nanoscale walls, enabling efficient energy dissipation and re-

sistance to dynamic impact fatigue.<sup>[38–40]</sup> Additionally, the fiber network within the pores plays a significant role in enhancing the aerogel's resilience. SEM images (Figure S9, Supporting Information) show that a portion of the fiber network is distributed among the pores, effectively dispersing compressive stress and providing additional cushioning and support. Furthermore, UL94 vertical burning tests confirmed that the aerogel achieves V-0 grade flame retardancy (Table S2, Supporting Information). No open flames or glowing embers were detected after multiple ignition attempts (Movie S5, Supporting Information).

## 2.2. Analysis of the EMW Absorption Properties of the G-PI@F<sub>20</sub>/CNT<sub>x</sub>

### 2.2.1. Analysis of EMW Absorption Performance of Thermal Reduction Samples at 400 and 600 °C

Through experimental optimization, the G-PI@F<sub>20</sub>/CNT<sub>x</sub> was refined. When the GO concentration was 2.5 mg mL<sup>-1</sup>, and the PI fiber and Fe<sub>3</sub>O<sub>4</sub> nanoparticle contents were 50% and 20% of the GO mass, respectively, the aerogel achieved an optimal balance between impedance matching and attenuation capability. Additionally, by adjusting the CNT content and thermal reduction temperature, the electromagnetic parameters of the aerogel were further tuned to enhance EMW absorption performance. The aerogel samples were thermally reduced at 400, 500, and 600 °C, with the 500 °C sample exhibiting the most favorable EMW absorption properties. Furthermore, the EMW absorption performance of aerogel samples following compression cycling was analyzed in detail in this section. Initially, the EMW absorption properties of aerogel samples thermally reduced at 400 and 600 °C were examined. Sample numbering is provided in Table 1 of the experimental section. The aerogel samples' electromagnetic parameters within the 2–18 GHz range were measured using a vector network analyzer (VNA). Reflection loss (RL) values were calculated using Equations S1, S2 (Supporting Information) based on transmission line theory.<sup>[3]</sup>

Figure 3a–c shows the RL curves for samples A1, A2, and A3, analyzed for their EMW absorption performance. With increasing CNT content, EMW absorption properties first improve and then decline. Figure 3d summarizes the RL<sub>min</sub> and corresponding EAB values for the three samples. The RL<sub>min</sub> values for A1, A2, and A3 are –48.81 dB (3.1 mm), –64.68 dB (2.5 mm), and –23.19 dB (2.4 mm), respectively, with corresponding EAB values of 7.42, 5.02, and 5.12 GHz. At thicknesses of 3.1–3.2 mm, A1, A2, and A3 achieve EAB<sub>max</sub> values of 8.30, 8.16, and 8.34 GHz, respectively, covering the entire Ku-band. In general, the real parts ( $\epsilon'$  and  $\mu'$ ) of the complex permittivity ( $\epsilon_r = \epsilon' - j\epsilon''$ ) and complex permeability ( $\mu_r = \mu' - j\mu''$ ) represent the storage capacity of electrical and magnetic energy, while the imaginary parts ( $\epsilon''$  and  $\mu''$ ) correspond to their respective energy dissipation capabilities. The trends of  $\epsilon'$  and  $\epsilon''$  are shown in Figure 3e. The observed order of values (A3 > A2 > A1) can be explained using free electron theory and effective medium theory.<sup>[8,41]</sup> As the CNT mass ratio increases, electron migration becomes more efficient, enhancing conduction loss. The  $\epsilon'$  values for all samples decrease with increasing frequency, which can be attributed to polarization hysteresis at higher frequencies. Figure 3f illustrates that  $\mu'$  and  $\mu''$  fluctuate around 1 and 0, respectively, in the 6–18 GHz range, indicating minimal magnetic loss. However, a distinct resonance peak is observed in the 2–6 GHz range, possibly related to enhanced exchange resonance. Additionally, the dielectric loss tangent ( $\tan \delta_E = \epsilon''/\epsilon'$ ), the magnetic loss tangent ( $\tan \delta_M = \mu''/\mu'$ ), and the attenuation constant  $\alpha$  (Equation S3, Supporting Information) were utilized to assess the EMW dissipation capability of the materials. The results show that  $\tan \delta_E$  values are higher than  $\tan \delta_M$  values for all samples (Figure S10, Supporting Information), indicating that dielectric loss is the dominant factor influencing EMW absorption. Among the samples, A3 demonstrates the highest dielectric loss capability in the high-frequency

range (8–18 GHz) and exhibits the strongest attenuation capability across the 2–18 GHz range (Figure S11, Supporting Information).

Figure 3g–i presents the RL curves for the samples thermally reduced at 600 °C. A significant reduction in EMW absorption performance is observed in samples D1, D2, and D3. The RL<sub>min</sub> values and corresponding EAB for these samples are provided in Figure 3j. Among them, D1 exhibits the highest absorption performance, with RL<sub>min</sub> and EAB<sub>max</sub> reaching –26.61 dB and 8.56 GHz, respectively. The variation trends of  $\epsilon'$  and  $\epsilon''$  for samples D1–D3 are similar to those of samples A1–A3. A substantial increase in the range of  $\epsilon'$  and  $\epsilon''$  values is observed (Figure 3k), indicating that adjusting the thermal reduction temperature effectively regulates the aerogels' dielectric constant. The  $\mu'$  and  $\mu''$  values display minor oscillatory changes across the 2–18 GHz frequency range (Figure 3l). From the trends of  $\tan \delta_E$ ,  $\tan \delta_M$ , and the attenuation constant  $\alpha$  (Figures S12 and S13, Supporting Information), it is evident that increasing CNT content and thermal reduction temperature enhance the overall attenuation capacity of the samples for EMW.<sup>[21]</sup> However, this also deteriorates impedance matching, leading to increased interfacial reflection and a subsequent decline in EMW absorption performance.<sup>[22]</sup> A similar trend is observed in the 2D impedance matching degree plot of the samples (Figure S14, Supporting Information).

### 2.2.2. EMW Absorption Performance of 500 °C Thermally Reduced Samples and the Impact of Compression Cycles on Properties

Given its remarkable compressive elasticity, G-PI@F<sub>20</sub>/CNT<sub>x</sub> may undergo multiple cyclic compressions in real-world applications. Therefore, it is essential to examine the impact of repeated compression on its EMW absorption performance. For instance, when used as a stealth layer on the backside of a solar panel (Figure S15, Supporting Information), the aerogel undergoes compression-recovery cycles during transitions between deployed and folded states (Figure 4a). To evaluate the stability of its EMW absorption properties, electromagnetic parameters were measured and compared between an uncompressed sample and a sample subjected to 1000 cyclic compressions at room temperature. By analyzing their EMW absorption performance, the structural stability of the aerogel was assessed. All tested samples underwent thermal reduction at 500 °C.

Initially, the electromagnetic parameters of the uncompressed aerogel samples B1, B2, and B3 were measured in the 2–18 GHz range to investigate their EMW absorption performance. Figure 4b–d shows the 3D RL diagrams for these samples. Sample B1 achieved an RL<sub>min</sub> of –70.34 dB at 10.96 GHz with a thickness of 3.7 mm, and the corresponding EAB was 6.92 GHz. At a thickness of 3.3 mm, B1 attained an EAB<sub>max</sub> of 8.34 GHz (9.66–18 GHz). For sample B2, an RL<sub>min</sub> of –60.3 dB was recorded at 14.74 GHz with a thickness of 3 mm and an EAB of 7.92 GHz. Increasing the thickness to 4.6 mm expanded the EAB<sub>max</sub> to 11.98 GHz (6.02–18 GHz), covering both the X-band and Ku-band. Compared to B1 and B2, sample B3 exhibited a lower RL<sub>min</sub> of –29.51 dB, while its EAB<sub>max</sub> reached 8.40 GHz. Figure 4e summarizes the relationship between EAB and thickness for sample B2, demonstrating that within the thickness range of 3.6–4.6 mm, an EAB exceeding 10 GHz was maintained.



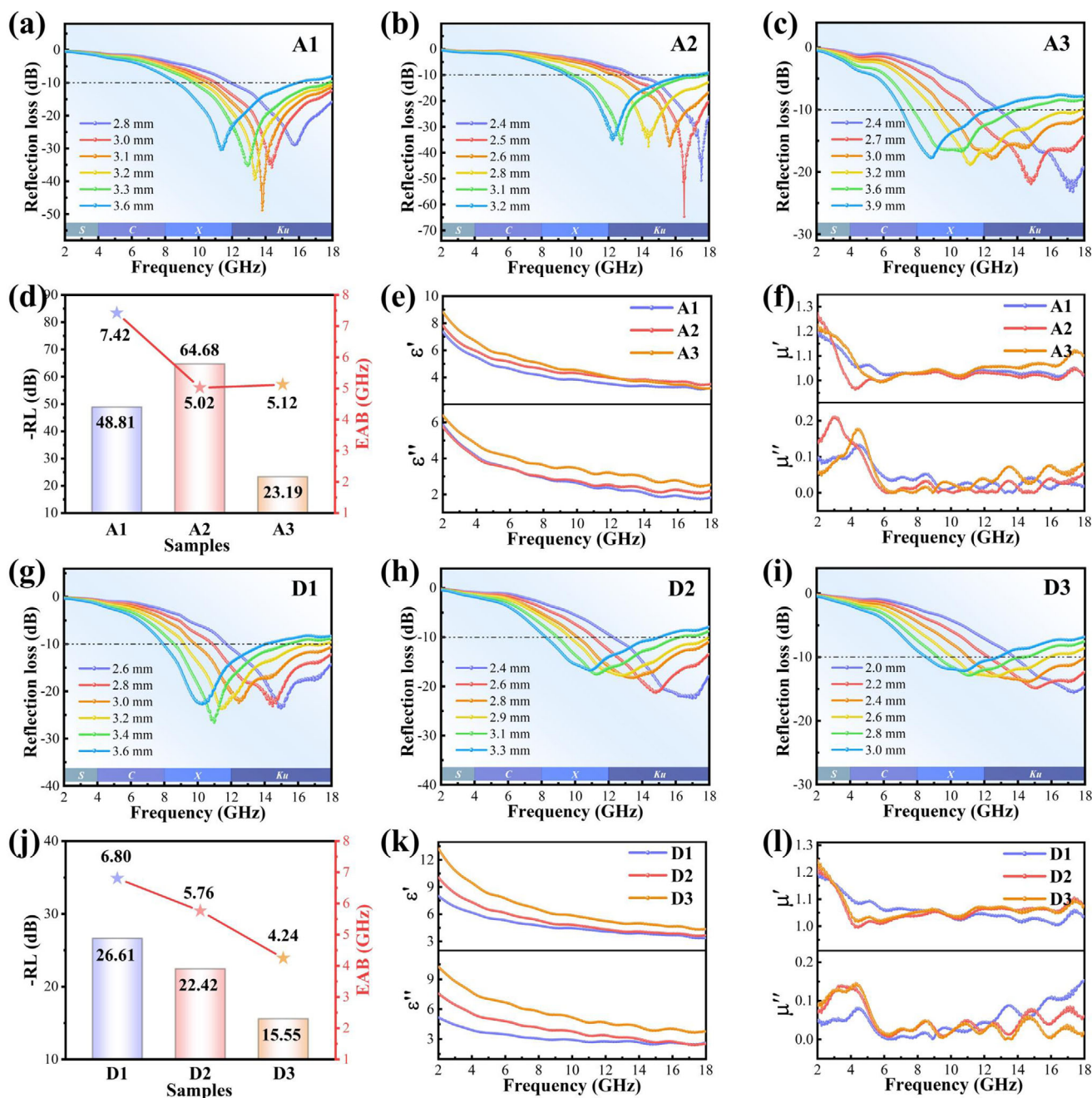


**Figure 3.** EMW absorption performance analysis of G-PI@F<sub>20</sub>/CNT<sub>x</sub> ( $x = 2, 4, 6$ ). Samples thermally treated at 400 °C (A1–A3): a–c) RL curves, d)  $RL_{\min}$  and corresponding EAB, e, f) Trends in the real and imaginary parts of complex permittivity and complex permeability. Samples thermally treated at 600 °C (D1–D3): g–i) RL curves, j)  $RL_{\min}$  and corresponding EAB, k, l) Trends in the real and imaginary parts of complex permittivity and complex permeability.

Figure 4f provides an overview of the  $RL_{\min}$  values and corresponding EAB values for the three samples.

Further analysis of the electromagnetic parameters of the samples within the 2–18 GHz frequency range was conducted. As shown in Figure 4g, the real part of the permittivity ( $\epsilon'$ ) for B1, B2, and B3 varies within the ranges of  $\approx 7.21$ – $3.18$ ,  $8.15$ – $3.01$ , and  $9.19$ – $3.47$ , respectively. The imaginary part of permittivity ( $\epsilon''$ ) falls within  $4.54$ – $1.93$ ,  $6.23$ – $2.02$ , and  $5.99$ – $2.47$ , respectively. The

observed decrease in  $\epsilon'$  with increasing frequency is attributed to the frequency dispersion effect, which results from the delayed response of electric dipoles in an alternating electric field. Among the samples, B3 exhibits the highest values for both real and imaginary parts of permittivity. To further assess the dielectric dissipation capability, the  $\tan \delta_E$  values were analyzed, as shown in Figure S16a (Supporting Information). The results indicate that  $\tan \delta_E$  for B2 follows an oscillatory decay trend in the

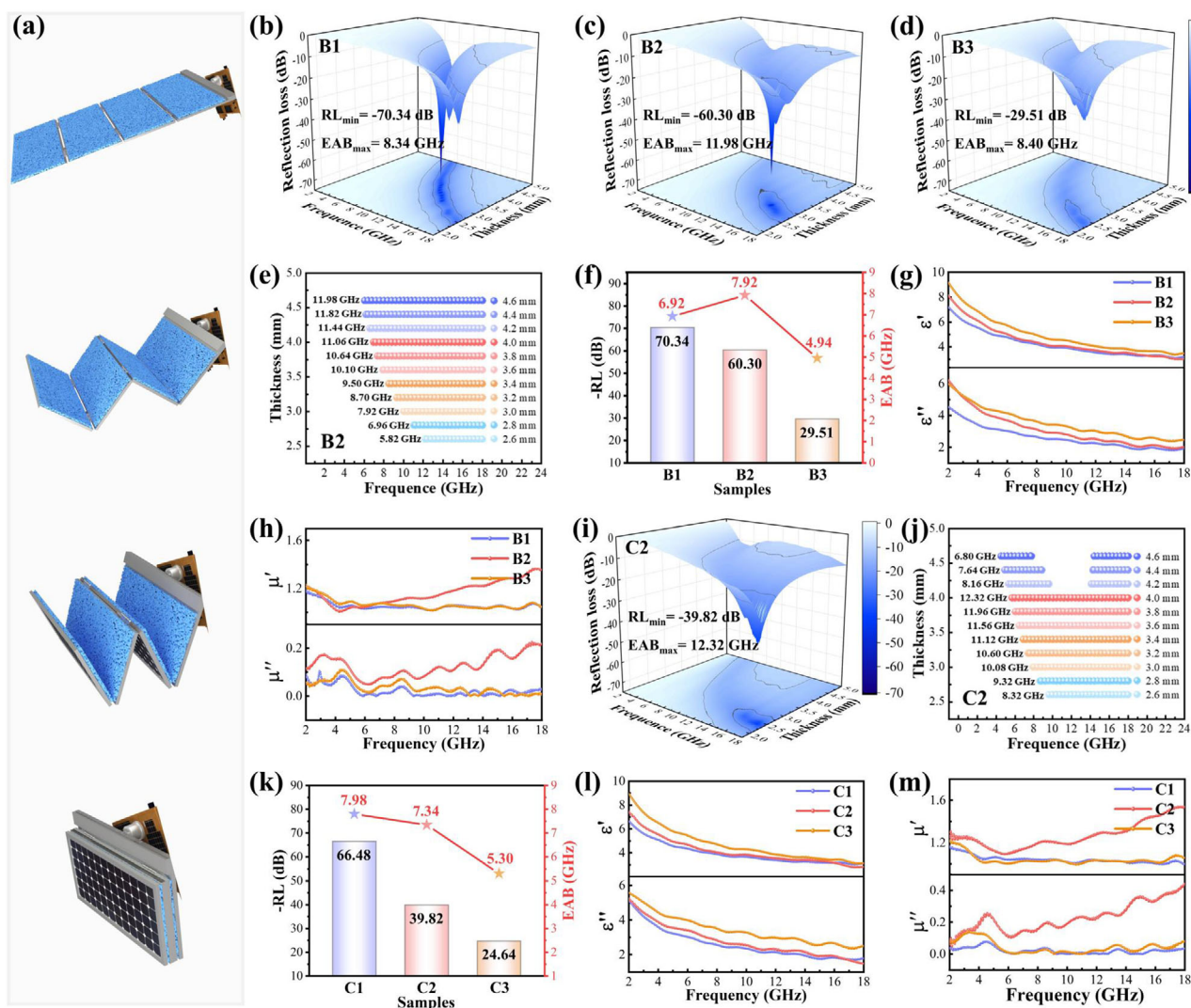


**Figure 4.** a) Schematic representation of the solar sail panel folding process with the aerogel layer. Samples thermally treated at 500 °C without compression (B1–B3): b–d) 3D RL value plots, e) EAB of B2 within the 2.6–4.6 mm range, f) RL<sub>min</sub> values and corresponding EAB, g) ε' and ε'' values, h) μ' and μ'' values. Samples subjected to 1000 compression cycles (C1–C3): i) 3D RL value plots, j) EAB of C2 within the 2.6–4.6 mm range, k) RL<sub>min</sub> values and corresponding EAB, l) ε' and ε'' values, m) μ' and μ'' values.

6–18 GHz range, signifying a reduction in dielectric loss capability with increasing frequency. In contrast, B1 and B3 exhibit relatively stable dielectric loss characteristics across the entire 2–18 GHz range. The frequency dependence of complex permeability is presented in Figure 4h. The μ' values for B1, B2, and B3 range from 1.04–1.19, 1.01–1.37, and 1.05–1.23, respectively, showing minimal variation. In this material system, magnetic storage is not the dominant factor contributing to EMW attenuation. The μ'' values were recorded as 0.00–0.10, 0.05–0.23, and 0.00–0.11 for B1, B2, and B3, respectively. In the high-frequency region (10–18 GHz), μ'' for B1 and B3 shifts toward negative values, suggesting a crossover effect between magnetic and electric energy in this range. Among the samples, B2 exhibits the highest μ'' values, with fluctuations across the frequency spectrum and multiple distinct resonance peaks, indicating that magnetic loss primarily originates from natural ferromagnetic resonance,

where agglomerated Fe<sub>3</sub>O<sub>4</sub> particles enhance interparticle coupling. The magnetic loss capability was further examined using tan δ<sub>M</sub> values (Figure S16b, Supporting Information). For B1 and B3, tan δ<sub>M</sub> exhibits an oscillatory decreasing trend with increasing frequency, while B2 shows an oscillatory increasing trend in the 6–18 GHz range. Notably, while the dielectric loss capability of B2 declines in this frequency range, its magnetic loss capability is significantly enhanced, leading to the formation of an effective electromagnetic synergistic loss mechanism.

Typically, Debye theory is applied to evaluate the dielectric loss, which includes both polarization and conductive losses (Equations S4–S6, Supporting Information).<sup>[42]</sup> The Cole–Cole semicircles observed for B1, B2, and B3 indicate the presence of dipole and interfacial polarization losses, while the slope of the curve tail reflects the conductive loss of the material (Figure S17, Supporting Information). This suggests that the aerogel effectively



enhances both polarization and conductivity. To further analyze the magnetic loss mechanism, the eddy current coefficient ( $C_0$ ) was examined (Equation S7, Supporting Information). As presented in Figure S18 (Supporting Information), the  $C_0$  values for B1, B2, and B3 stabilize rapidly with increasing frequency, forming an about linear trend in the 6–18 GHz range. This result indicates that eddy current loss is the dominant magnetic loss mechanism in this frequency range. Therefore, in the low-frequency region, the primary contributors to magnetic loss are the exchange and natural resonances of  $\text{Fe}_3\text{O}_4$  nanoparticles. Although the aerogel system does not exhibit particularly strong magnetic loss characteristics, the  $\text{Fe}_3\text{O}_4$  nanoparticles dispersed along the pore walls enhance impedance matching, thereby improving the efficiency of EMW incidence. The overall dissipation capability of B1, B2, and B3 was assessed using the attenuation constant  $\alpha$  (Figure S19, Supporting Information). The results indicate that an increase in CNT content leads to higher  $\alpha$  values ( $B3 > B2 > B1$ ), signifying enhanced EMW dissipation capability. However, B3 exhibits relatively lower EMW absorption performance. This discrepancy arises because EMW absorption performance is not solely dependent on dissipation capability; rather, effective impedance matching is crucial for optimal absorption, necessitating further investigation.<sup>[43]</sup>

The variation trend of the impedance matching degree ( $Z$ ) was calculated, as illustrated in Figure S20 (Supporting Information). Typically, a  $Z$  value within the range of 0.8–1.2 is considered an indicator of good impedance matching (Equation S8, Supporting Information).<sup>[44]</sup> Among the samples, B2 exhibits the widest matching region, suggesting that EMW can efficiently penetrate the aerogel's interior and undergo balanced attenuation. In contrast, when the  $Z$  value exceeds the optimal impedance matching range, a significant portion of EMW may be reflected at the air-aerogel interface, thereby reducing EMW absorption efficiency. Furthermore, as thickness increases, the absorption peak shifts toward lower frequencies, indicating that the G-PI@ $\text{Fe}_3\text{O}_4$ /CNT<sub>x</sub> material follows the quarter-wavelength theory (Equation S9, Supporting Information). The Smith impedance charts for B1–B3 (Figure S21, Supporting Information) further confirm that as thickness increases, the impedance curves shift toward the matching region. These findings collectively demonstrate that the hierarchical porous structure of the aerogel optimizes the dielectric constant and impedance matching, enhances interfacial polarization and multiple scattering, and promotes the penetration and attenuation of EMW.

To examine the impact of compression cycling on the EMW absorption performance of the material, electromagnetic parameters were evaluated for aerogel samples C1, C2, and C3, which underwent 1000 compression cycles at room temperature. The results indicate that C1, C2, and C3 have comparable EMW absorption performance to B1, B2, and B3. Among these samples, C1 exhibits an  $\text{RL}_{\min}$  of  $-66.48$  dB and a corresponding EAB of 7.98 GHz (Figure S22a, Supporting Information). Sample C2 achieves an EAB<sub>max</sub> of 12.34 GHz (5.66–18 GHz) at 4 mm thickness, covering most of the C-band and the entire X- and Ku-bands (Figure 4i). Sample C3 demonstrates performance similar to B3, with  $\text{RL}_{\min}$  and EAB<sub>max</sub> values of  $-24.64$  dB and 8.98 GHz, respectively (Figure S22b, Supporting Information). Figure 4j summarizes the relationship between EAB and thick-

ness for C2, indicating that an EAB exceeding 10 GHz can be maintained within the 3.0–4.0 mm thickness range. The  $\text{RL}_{\min}$  values and corresponding EAB for C1, C2, and C3 are presented in Figure 4k. Based on the findings, after compression cycling, the  $\text{RL}_{\min}$  values of the samples exhibit slight attenuation, while the EAB experiences a slight expansion. This change is attributed to structural modifications within the aerogel during compression. High compressive stress and deformation affect the tightly stacked pore walls, causing fragmentation of locally agglomerated reduced graphene oxide lamellae. This process results in a more uniform conductivity and dielectric distribution within the aerogel. The 2D impedance matching plots of C1, C2, and C3 further illustrate this phenomenon (Figure S23, Supporting Information), showing an extension of the impedance matching region compared to the uncompressed samples. Notably, C2 exhibits a significantly broader impedance-matching region than B2, correlating with its expanded EAB.

The variations in complex permittivity for C1, C2, and C3 were further examined (Figure 4l). The  $\epsilon'$  values range from 6.66–3.11, 7.46–2.82, and 8.97–3.11, and the  $\epsilon''$  values range from 5.15–1.78, 5.25–1.48, and 5.57–2.50 for C1, C2, and C3, respectively. Compared to the uncompressed samples, these values show a slight decrease, aligning with the hypothesis that the conductivity and dielectric properties within the aerogel become more uniform after compression. Since the magnetic component content remains identical across the samples, variations in  $\mu'$  and  $\mu''$  are minimally influenced by the compression process (Figure 4m). The primary difference from uncompressed samples is a more pronounced increase in  $\mu''$  for C2. However, the overall fluctuation trends of  $\mu'$  and  $\mu''$  remain consistent with those in uncompressed samples. Comparison of Cole–Cole plots and loss tangent values of compressed and uncompressed samples (Figures S24, and S25, Supporting Information) shows that the loss mechanisms remain unchanged after compression. The dielectric loss capacity remains similar, whereas the magnetic loss capacity shows a slight enhancement. This enhancement is attributed to the more uniform distribution of  $\text{Fe}_3\text{O}_4$  particles within the aerogel and structural modifications induced by compression cycles. Slight variations in  $C_0$  values (Figure S26, Supporting Information) indicate increased contributions of exchange resonance and natural resonance of  $\text{Fe}_3\text{O}_4$  particles in the low-frequency region, while eddy current loss continues to dominate in the high-frequency region. The overall loss capability was evaluated using  $\alpha$  (Figure S27, Supporting Information), where C2 and B2 exhibit comparable  $\alpha$  values, achieving well-balanced impedance matching and loss capability. Overall, the aerogel structure remains highly stable after 1000 compression cycles at room temperature, maintaining excellent EMW absorption performance. This remarkable fatigue resistance provides a significant advantage for applications in demanding environments.

### 2.3. Simulation and Verification

With the continuous advancement of space technology, artificial satellites have become essential for communications, meteorology, reconnaissance, navigation, space exploration, and national defense. However, the rapid progress of modern radar detection

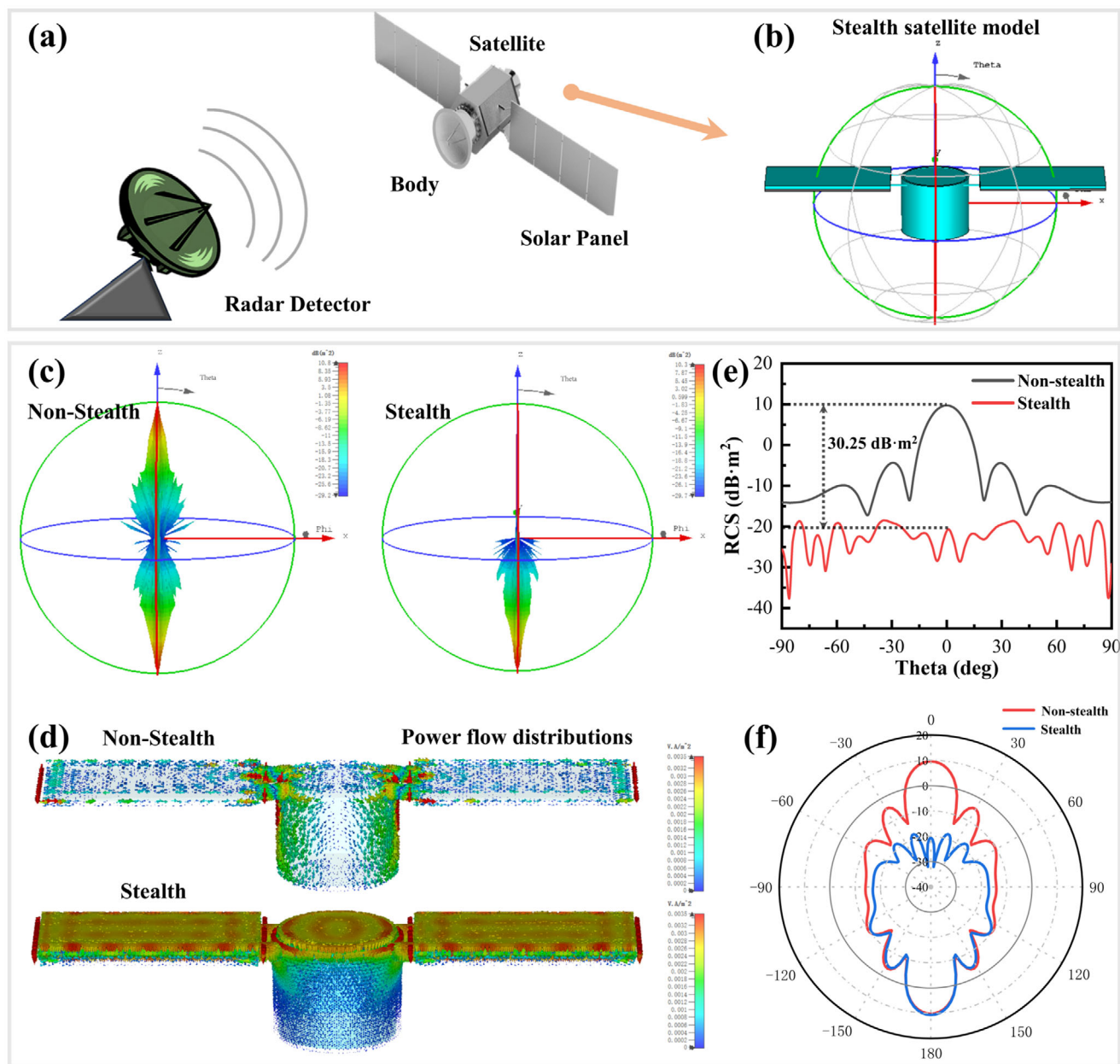


**Figure 5.** a) Schematic diagram of a satellite being detected by radar. b) Satellite micro-model covered with a B2 skin layer ( $4\text{ mm}$ ,  $4.35\text{ mg cm}^{-3}$ ). c) 3D scattering signal and d) absorption-related energy flow distributions of non-stealth and stealth satellites. e) Monostatic RCS simulation of non-stealth and stealth satellites across different PW angles ( $-90^\circ$  to  $90^\circ$ ) at a monitoring wavelength of  $14.74\text{ GHz}$ . f) RCS radiation signal distributions.

technologies poses an increased risk of satellites being detected, jammed, or even targeted for destruction. As a result, the development of stealth technology to improve the survivability of artificial satellites has become a critical necessity (Figure 5a).<sup>[45]</sup> Due to its broadband compatibility and strong absorption capabilities, the G-PI@F<sub>20</sub>/CNT<sub>x</sub> absorber presents significant potential for electromagnetic protection in space environments. In this study, simulation software was employed to design a satellite micro-model (Figure 5b), which consists of a satellite body and a solar panel. Sample B2 was utilized as a stealth layer to investigate its potential applications in stealth satellite technology. CST Studio Suite

2022 was employed to evaluate the RCS across different plane wave (PW) incident angles and frequencies within the 2–18 GHz range.

Initially, RCS simulations were performed on the satellite model (Equation S10, Supporting Information) to assess the attenuation effect of the aerogel stealth coating on the satellite's RCS signal. Within the 2–18 GHz frequency range, the stealth layer converts EMW energy into other forms through a synergistic loss mechanism. In the simulation model, this process is reflected in the formation of electric and magnetic field energy flows within the stealth layer. As illustrated in the 3D radar wave

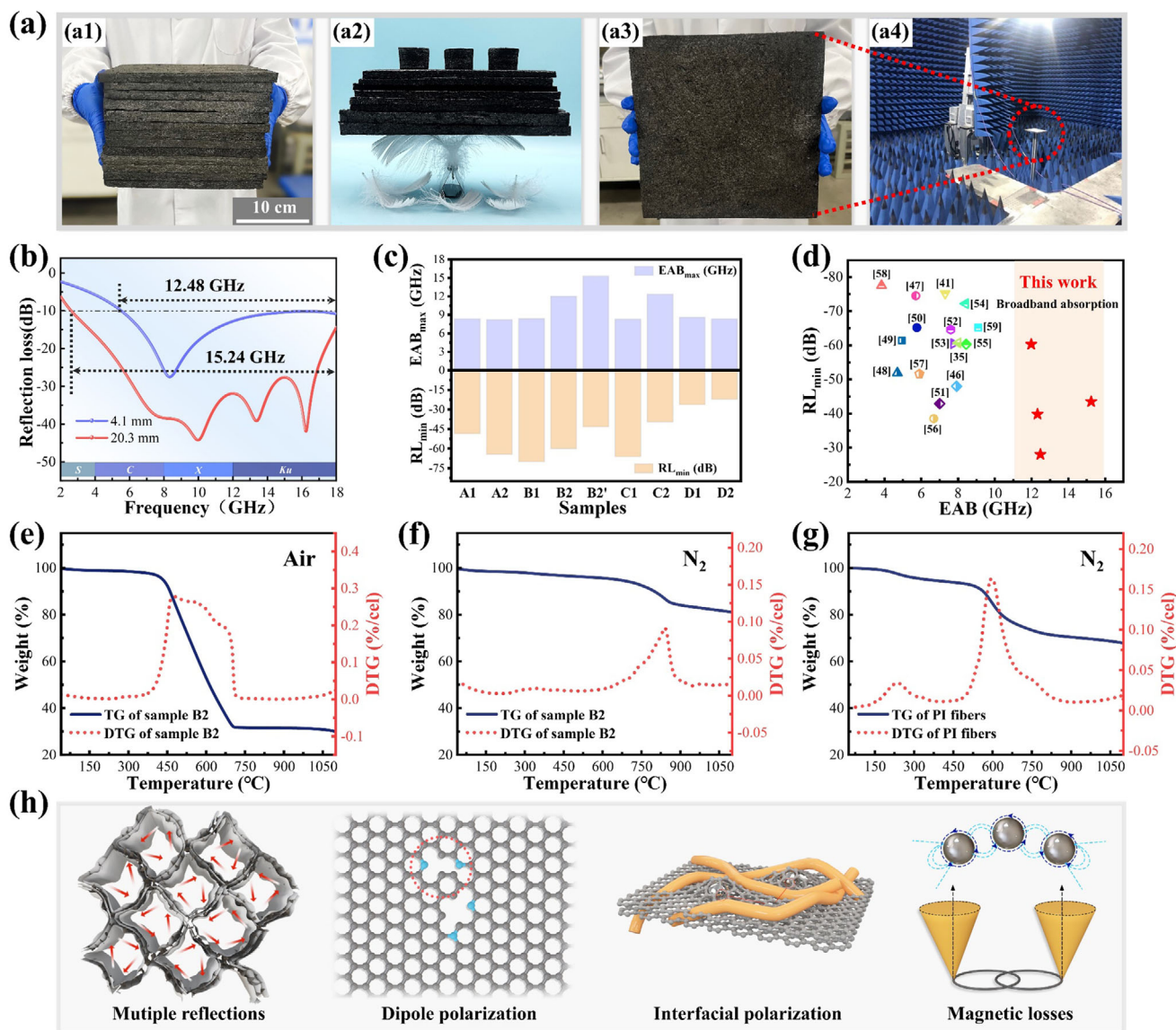


**Figure 6.** a) Test samples and testing site. b) RL curves of B2'. c) Summary of RL<sub>min</sub> and EAB<sub>max</sub> for all test samples. d) Comparison of RL<sub>min</sub> and EAB<sub>max</sub> of different graphene-based EMW absorbing materials that have been reported. e) TG curve of B2 in an air atmosphere. TG curve of f) B2 and g) PI fibers in a nitrogen atmosphere. h) EMW loss mechanism of the G-PI@F<sub>20</sub>/CNT<sub>x</sub>.

scattering signals of non-stealth and stealth satellites (Figure 5c), the B2 stealth layer effectively reduces scattering signals. This effect is attributed to its superior impedance matching and electromagnetic synergistic loss mechanism, which enhances radar wave attenuation efficiency. This is further supported by the gradual increase in absorption-related energy flow at the satellite surface (Figure 5d). Additionally, RCS signals measured at different PW incident angles and a monitoring wavelength of 14.74 GHz demonstrate that the stealth layer significantly reduces the RCS signal. The RCS reduction is observed across nearly all PW angles from 0° to 180°, with a maximum reduction value of 30.25 dB·m<sup>2</sup> (Figure 5e). Furthermore, as depicted in the RCS radiation signal diagram (Figure 5f), the stealth layer substantially decreases the scattered signal intensity and display size, which is highly advantageous for improving satellite stealth capabilities.

Electromagnetic parameter simulations confirm that B2, when used as a stealth layer, effectively reduces the target RCS signal, thereby achieving a reliable stealth effect. To further validate the material's reliability, a scaled-up sample, B2', was fabricated using the same composition ratio as B2, with dimensions of 180 mm × 180 mm × *d*, where the thickness (*d*) varies from 3 to 25 mm (Figure 6a1–a2). The sample exhibits an ultralow density of 4.35 mg cm<sup>-3</sup> (Figure S28, Supporting Information), highlighting its exceptional lightweight characteristics, which are highly suitable for EMW absorbing materials. Notably, multiple aerogel samples can be supported by just two feathers, emphasizing their lightweight advantage. The TM wave absorption performance of B2' was evaluated in a microwave darkroom using the bow method, with the test samples and setup shown in Figure 6a3–a4. The results indicate that at a sample thickness



of 4.1 mm, the  $RL_{\min}$  reaches  $-28.03$  dB at 8.35 GHz, with an EAB of 12.48 GHz (Figure 6b), which aligns well with results obtained using the coaxial method. Increasing the aerogel thickness to 20.3 mm significantly enhances both EAB and  $RL_{\min}$ . At 9.97 GHz,  $RL_{\min}$  reaches  $-43.49$  dB, with an expanded EAB of 15.24 GHz (2.76–18 GHz), covering the entire C, X, and Ku bands and most of the S-band, thereby achieving multi-spectrum absorption. The bow method results further confirm the aerogel's strong and stable EMW absorption performance, demonstrating its substantial application potential. Summarizing the findings, the optimal EMW absorption performance is achieved when the CNT content is 20% or 40%. Figure 6c and Table S3 (Supporting Information) provide an overview of the  $RL_{\min}$  and EAB values for all tested samples, illustrating that the aerogel system consistently achieves an EAB exceeding 7 GHz. When compared to the performance of graphene-based aerogels reported in the literature (Figure 6d; Table S4, Supporting Information),<sup>[35,41,46–59]</sup> this aerogel system exhibits superior multi-spectrum EMW absorption capabilities, offering significant advantages for stealth applications.

Additionally, thermogravimetric (TG) tests were performed on sample B2 under air and nitrogen atmospheres to assess the thermal stability of the aerogel system (Figure 6e). In an air atmosphere, significant weight loss begins at  $\approx 410$  °C, with a residual mass of 32% remaining at  $\approx 705$  °C. Under a nitrogen atmosphere, accelerated weight loss occurs at  $\approx 610$  °C (Figure 6f), with a total mass loss of 4.2%, primarily attributed to the decomposition of oxygen-containing functional groups, residual moisture, and slow dehydrogenation and deoxygenation condensation reactions. The PI fiber network in a nitrogen atmosphere begins to undergo significant decomposition at  $\approx 440$  °C, with a recorded mass loss of 6.4% (Figure 6g). This mass loss is mainly due to dehydrogenation and deoxygenation condensation reactions occurring on the surface of modified PI fibers, leading to the release of CO, CO<sub>2</sub>, and H<sub>2</sub>. Considering these results, the aerogel system demonstrates structural stability over a wide temperature range, confirming its excellent thermal resistance for practical applications.

Based on experimental and simulation analyses, the EMW absorption mechanism of the aerogel system is elucidated, demonstrating that its excellent absorption performance results from multiple factors (Figure 6h). The hierarchical porous structure, defect engineering, heterointerface design, and electromagnetic coupling mechanism enable the composite aerogel to achieve high-efficiency EMW absorption while maintaining an ultrathin and lightweight structure. G-PI@F<sub>20</sub>/CNT<sub>x</sub> incorporates pore unit structures of varying sizes, creating multiple reflection spaces for incident EMW.<sup>[41,57]</sup> This enhances EMW interaction with structural units, leading to multiple reflections and strong scattering, which extend the propagation path of incident waves and facilitate their attenuation by converting electromagnetic energy into heat or other dissipative forms. Additionally, the layered structure of the pore walls introduces multiple interfaces, enhancing interfacial polarization. The interconnected rGO pore walls form a conductive network. This facilitates rapid electron transport, improving conductivity and increasing conduction loss. Additionally, residual functional groups and defects on rGO, CNTs, and PI fibers induce defect polarization and electron dipole relaxation. Charge accumulation near de-

fects disrupts local electronic structural symmetry, increasing the density of intrinsic dipoles.<sup>[46,48]</sup> Under an external electromagnetic field, the orientational oscillation of these dipoles enhances dipolar polarization loss. Additionally, uniformly dispersed Fe<sub>3</sub>O<sub>4</sub> nanoparticles within the pore walls serve as magnetic loss sites, generating magnetic loss and effectively modulating the electromagnetic synergy mechanism.<sup>[2,6]</sup> Ultimately, the unique layered porous structure and multiple loss mechanisms work synergistically to achieve a delicate balance between impedance matching and energy dissipation. This balance enables G-PI@F<sub>20</sub>/CNT<sub>x</sub> to achieve broadband and efficient EMW absorption.

## 2.4. Verification and Analysis of Multifunctional Application Scenarios

In the extreme environment of space, both thermal and electromagnetic protection are crucial for detection equipment. The G-PI@F<sub>20</sub>/CNT<sub>x</sub> material, which integrates both exceptional properties, was tested and evaluated under simulated extreme temperature conditions to validate its thermal insulation and EMW absorption performance. Figure 7a illustrates the components utilized for assessing EMW absorption performance, including a spectrum analyzer, EMW signal source, directional transmitting antenna, near-field receiving antenna, signal amplifier, and signal transmission lines. The experimental setup, shown in Figure 7b, consists of three main sections: thermal preservation in extreme low-temperature conditions, thermal insulation in high-temperature environments, and demonstration of EMW absorption performance.

For the EMW absorption demonstration, an aluminum backing plate was positioned directly above the signal-emitting end of the directional antenna. The EMW signal source was configured to emit a 5.5 GHz EMW. In the absence of the aerogel layer, the EMW was reflected off the aluminum surface, and the near-field receiving antenna detected the vertically reflected waves, producing a prominent 5.5 GHz signal peak on the spectrum analyzer (Figure 7c1). Subsequently, a B2' sample with dimensions of 180 × 90 × 10 mm was placed beneath the aluminum backplane. As observed in Figure 7c2, the 5.5 GHz signal peak on the spectrum analyzer nearly disappeared. This result confirms that the aerogel layer effectively attenuates the reflected signal generated by EMW at the interface, significantly reducing reflection intensity.

In space, the temperature difference between the sunlit and shadowed sides can exceed 300 °C, presenting a significant challenge in ensuring the stable operation of electronic devices under extreme thermal conditions. To further evaluate the aerogel's protective performance in ultralow and high-temperature environments, experiments were conducted using liquid nitrogen as a refrigerant medium to create a  $-196$  °C ultralow temperature environment. Temperature sensors were installed on both sides of a 10 mm thick aerogel sample, which was then positioned on a copper block cooled by liquid nitrogen. These sensors monitored the dynamic temperature changes on both surfaces of the aerogel. To simulate a high-temperature radiation environment, a 160 °C heating stage was used, with identical temperature sensors tracking the aerogel's surface temperature changes. After

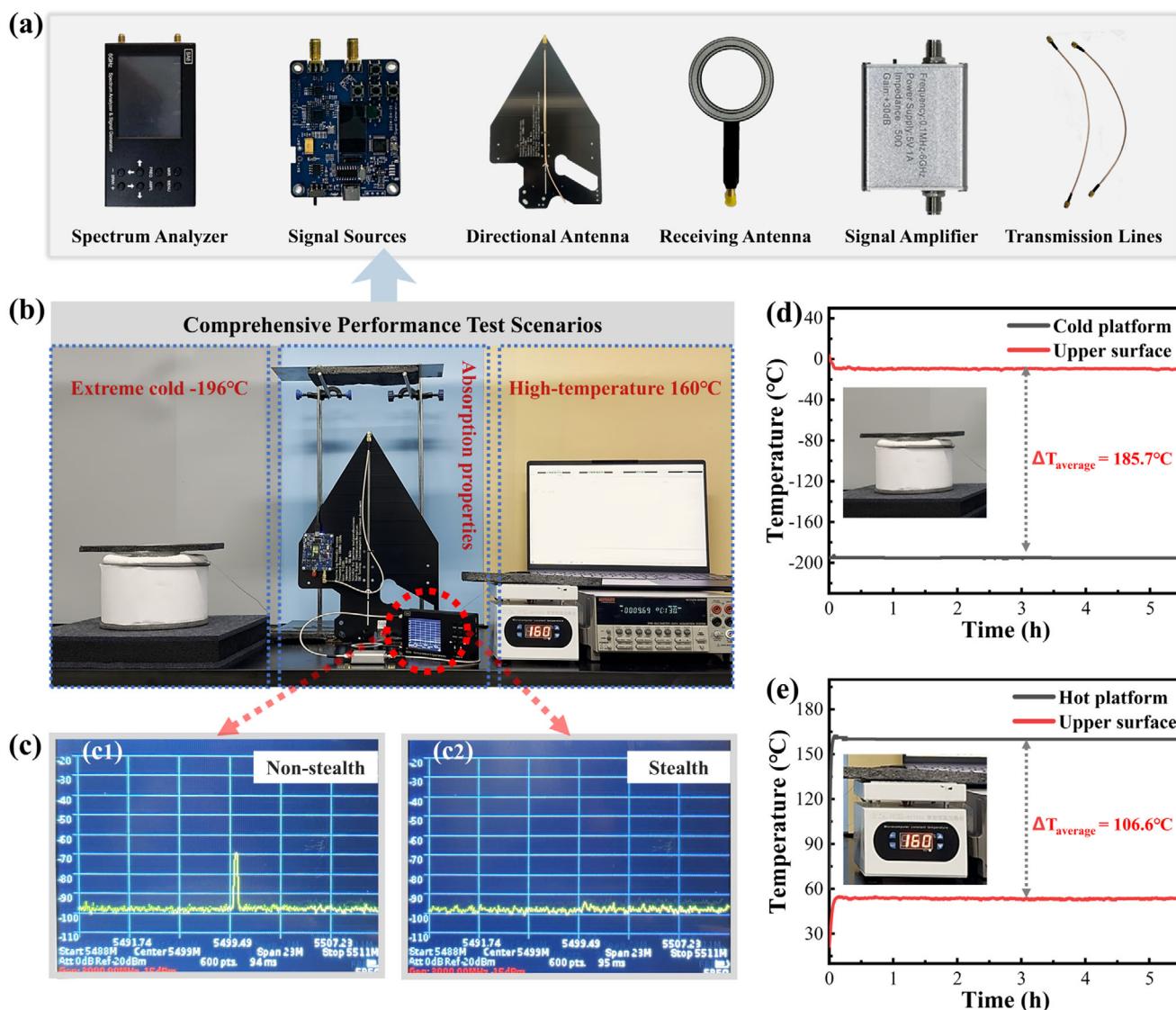


**Figure 7.** a) Components of the EMW absorption performance demonstration. b) Scenario demonstration and validation of the aerogel's comprehensive performance. c) Spectrum analyzer signal display before and after aerogel coverage. d) Surface temperature fluctuation curve of the aerogel under ultralow temperature conditions. e) Surface temperature fluctuation curve of the aerogel under high-temperature conditions.

5.5 h of dynamic temperature monitoring, the surface temperatures of the aerogel samples remained stable under both extreme conditions, as illustrated in Figure 7d,e. In the  $-196^{\circ}\text{C}$  environment, the surface temperature of the aerogel rapidly stabilized around  $-10^{\circ}\text{C}$ , with an average temperature difference of  $185.7^{\circ}\text{C}$  between the upper and lower surfaces, confirming its high-efficiency thermal preservation in extreme cold. Similarly, in the  $160^{\circ}\text{C}$  high-temperature environment, the aerogel's surface temperature stabilized and fluctuated  $\approx 54^{\circ}\text{C}$ , maintaining an average temperature difference of  $106.6^{\circ}\text{C}$  between the upper and lower surfaces, demonstrating its excellent thermal insulation capability. To evaluate the influence of alternating temperature conditions on the aerogel's performance and electromagnetic properties, we measured the electromagnetic parameters at room temperature and under cyclic temperature conditions (1 h at high temperature:  $150^{\circ}\text{C}$ , and 1 h at low temperature:

$-130^{\circ}\text{C}$ , repeated for 12 h). The comparison revealed that the real and imaginary parts of both the complex permittivity and complex permeability remained relatively stable, with minimal performance variation (Figure S29, Supporting Information). These results confirm that the aerogel effectively provides thermal and electromagnetic protection under extreme temperature conditions, exhibiting stability under both low- and high-temperature shocks.

The thermal conductivity of the aerogel was further evaluated under different compression levels (Figure S30, Supporting Information). In its uncompressed state, the aerogel exhibited an ultralow thermal conductivity of  $0.0313\text{ W m}^{-1}\text{ K}^{-1}$ , confirming its exceptional thermal insulation performance. Infrared thermographic images captured during the heating process (Figure S31, Supporting Information) reveal that heat flow remained primarily confined to the lower one-third of the aerogel. This behavior

is attributed to its unique layered porous structure and multi-scale pore size distribution. The insulation mechanism of the aerogel is based on its hierarchical pore microstructure, which effectively suppresses air convection, minimizes thermal radiation, and reduces thermal conduction (Figure S32, Supporting Information).<sup>[60–62]</sup> Specifically, the presence of pores increases the heat transfer path, thereby lowering thermal conductivity. Meanwhile, air is trapped within the small pores, disrupting convection pathways and rendering convective heat transfer negligible. In addition, the solid–air interfaces within the pores facilitate multiple reflections of infrared radiation, further minimizing radiative heat loss. The comprehensive experimental demonstrations of the G-PI@F<sub>20</sub>/CNT<sub>x</sub> confirm its outstanding EMW absorption and thermal protection capabilities in extreme temperature environments. Even when exposed to conditions ranging from –196 to 160 °C, the aerogel ensures the stable operation of electronic devices within a temperature range of –10 to 54 °C, providing reliable long-term thermal and electromagnetic protection. This exceptional performance highlights the aerogel's considerable potential for aerospace applications.

### 3. Conclusion

The contradiction between the characteristics of multiple interfaces and their anti-fatigue performance of traditional graphene-based aerogels has been addressed by employing in situ PI welding technology. The as-prepared graphene aerogel with PI fiber cross-linked network could withstand 90% strain compression cycles over a wide temperature range (–196 to 160 °C) with less than 5% deformation loss. The aerogel with a unique hierarchical porous structure possesses an ultralow density of 4.35 mg·cm<sup>–3</sup>, achieving an EAB of 12.48 GHz at a thickness of 4.1 mm, and ultra-broadband absorption covering 2.76–18 GHz with an RL<sub>min</sub> of –43.49 dB at a thickness of 20.3 mm. The hierarchical porous structure could suppress phonon transport and air convection, yielding an ultralow thermal conductivity of 0.0313 W m<sup>–1</sup> K<sup>–1</sup>, as well as V-0 level flame retardancy. Overall, the G-PI@F<sub>20</sub>/CNT<sub>x</sub> material demonstrates significant potential for aerospace and other advanced applications due to its excellent ultra-elasticity, EMW absorption capabilities, thermal insulation, and flame retardancy. This study also serves as a valuable reference for solving the mechanical resilience problem of other nanomaterial assemblies in extreme environments.

### 4. Experimental Section

**Materials:** Multi-walled carbon nanotubes (98%) were purchased from Suzhou Tanfeng Graphene Technology Co., Ltd. Polyimide short fibers were purchased from Jiangsu Xfnano Materials Tech Co., Ltd. Sodium ascorbate (98%) were purchased from Shanghai Dobio Biotech Co., Ltd. Fe<sub>3</sub>O<sub>4</sub> nanoparticles (95%, 200 nm), potassium permanganate (99.7%), phosphorus pentoxide (99.9%), sodium nitrite (99.7%), sodium hydroxide (99.7%) were purchased from Xien Si Biochemical Technology Co., Ltd. Anhydrous ethanol (99.7%), hydrochloric acid, sulfuric acid were purchased from Jiangtian Chemicals Technology Co., Ltd. Graphene oxide was prepared using an improved Hummers' method, as reported by Yin et al.<sup>[20]</sup> Deionized water was prepared in the laboratory.

**Modification of Multi-Walled Carbon Nanotubes and Polyimide Short Fibers:** Ten grams of polyimide short fibers were evenly dispersed into

1 L of a 1 M NaOH solution, and the mixture was vigorously stirred at 40 °C in a water bath for 100 min. The treated polyimide short fibers were then thoroughly washed with deionized water until neutral, followed by freeze-drying to obtain hydrophilic polyimide fibers.

Carboxylated multi-walled carbon nanotubes were prepared using an improved Hummers method. Under the condition of a 60 °C oil bath, 12 g of phosphorus pentoxide was dissolved in 80 mL of concentrated sulfuric acid. Then, 2 g of multi-walled carbon nanotubes were added to a beaker, and the mixture was stirred and dispersed uniformly and then cooled. Subsequently, 5 g of potassium permanganate was slowly added under an ice bath, and the reaction was carried out for 2 h. The mixture was then transferred to a 40 °C oil bath for an additional 2 h of reaction. After the reaction, the product was washed to neutrality by centrifugation with deionized water, followed by freeze-drying to obtain carboxylated multi-walled carbon nanotubes (CNTs).

**Preparation of G-PI@F<sub>20</sub>/CNT<sub>x</sub> Aerogels:** Deionized water was used as the solvent, with the concentration of graphene oxide set at 2.5 mg mL<sup>–1</sup>. The proportion of each component in the precursor solution was based on the mass of GO. The contents of Fe<sub>3</sub>O<sub>4</sub> nanoparticles and PI fibers were 20% and 50% of the mass of GO, respectively. The CNTs content in different precursor solutions was 20%, 40%, and 60% of the mass of GO, while the sodium ascorbate content was 15% of the mass of GO. The samples were named G-PI@F<sub>20</sub>/CNT<sub>2</sub>, G-PI@F<sub>20</sub>/CNT<sub>4</sub>, and G-PI@F<sub>20</sub>/CNT<sub>6</sub>, corresponding to different CNTs contents. The components were weighed according to the above ratios and sequentially dispersed into deionized water, followed by uniform dispersion through sonication and mechanical stirring. The resulting mixture was then transferred to a hydrothermal reaction vessel and reacted at 110 °C for 12 h. The composite hydrogel obtained from the reaction was freeze-dried and then subjected to thermal reduction in a vacuum tube furnace. The heating rate was 5 °C min<sup>–1</sup>, and the holding time was 1 h, with final temperatures of 400, 500, and 600 °C, under a protective gas mixture of argon and hydrogen in a 10:1 volume ratio. The sample numbers for different contents and treatment conditions are shown in Table 1. In addition, large-sized samples were fabricated using a custom-made PTFE mold with dimensions of 25 × 25 × 5 cm, structurally resembling a square Petri dish, and equipped with internal sealing gaskets. The thermal reduction process for the large-sized samples was conducted in a vacuum box furnace, with all other conditions kept consistent with those used for the small-sized samples.

**Characterization:** Scanning electron microscopy (SEM) images were acquired using a Hitachi S4800 instrument. Transmission electron microscopy (TEM) images were recorded on a JEM-2100F microscope. X-ray energy-dispersive spectroscopy (EDS) was taken on a JEM-2010HR-Vantage energy spectrometer. X-ray photoelectron spectroscopy (XPS) was implemented on Thermo ESCA Lab250XI. The compression performance of samples at room temperature and ultralow temperature was tested using the xQ-46L electronic universal testing machine. The high-temperature compression performance of samples was tested in a QY-46L high and low-temperature test chamber (Shenzhen Baiying Technology Co., Ltd.). The specific surface area of nitrogen adsorption and desorption at 77 K was calculated using the Brunauer–Emmett–Teller (BET) method on an ASAP2460 adsorption system. Electromagnetic parameters in the frequency range of 2–18 GHz were analyzed using an N5232A vector network analyzer (Agilent Technologies, USA), with the sample being a ring with an inner diameter of 3.04 mm and an outer diameter of 7.00 mm. TM wave data for aerogel samples with dimensions of 180 × 180 × 4.1 mm and 180 × 180 × 20.3 mm were tested using a 3672C vector network analyzer (CETC Siyi Technology Co., Ltd.). The thermal conductivity of samples at compression rates of 0%, 30%, 60%, and 90% was measured using the heat flux method (TC2120E, XIATECH, China). Thermal infrared images of samples were obtained using an infrared thermal imager (TiX 660, Fluke, USA). The thermal insulation performance of samples was evaluated by collecting temperature changes on the upper and lower surfaces of the aerogel using a Keithley 2700 digital multimeter. The flame retardancy of samples was evaluated using an LSD-UL type horizontal and vertical flame tester. Thermogravimetric (TG) data is collected by Japanese Rigaku equipment.



## Supporting Information

Supporting Information is available from the Wiley Online Library or from the author.

## Acknowledgements

This work was financially supported by the National Key Research and Development Program of China (No. 2022YFB3805702) and the National Natural Science Foundation of China (Nos. 52173078, 52327802, 52130303, and 52303101).

## Conflict of Interest

The authors declare no conflict of interest.

## Data Availability Statement

The data that support the findings of this study are available in the supplementary material of this article.

## Keywords

electromagnetic wave absorption, extreme temperature, graphene aerogels, superelasticity, thermal insulation

Received: April 2, 2025

Revised: April 21, 2025

Published online:

- [1] X. Zhou, P. Min, Y. Liu, M. Jin, Z. Yu, H. Zhang, *Science* **2024**, 385, 1205.
- [2] M. He, X. Zhong, X. Lu, J. Hu, K. Ruan, H. Guo, Y. Zhang, Y. Guo, J. Gu, *Adv. Mater.* **2024**, 36, 2410186.
- [3] X. Liu, W. Ma, Z. Qiu, T. Yang, J. Wang, X. Ji, Y. Huang, *ACS Nano* **2023**, 17, 8420.
- [4] W. Gu, J. Sheng, Q. Huang, G. Wang, J. Chen, G. Ji, *Nano-Micro Lett.* **2021**, 13, 102.
- [5] K. Ruan, X. Shi, Y. Zhang, Y. Guo, X. Zhong, J. Gu, *Angew. Chem., Int. Ed.* **2023**, 62, 202309010.
- [6] H. Lv, Z. Yang, H. Pan, R. Wu, *Prog. Mater. Sci.* **2022**, 127, 100946.
- [7] Y. Li, C. Dong, S. Wang, P. Zhang, D. Lei, B. Yin, Z. Chen, X. He, C. Liu, J. Liu, *Mater. Today Phys.* **2024**, 42, 101373.
- [8] J. Xiao, B. Zhan, M. He, X. Qi, Y. Zhang, H. Guo, Y. Qu, W. Zhong, J. Gu, *Adv. Funct. Mater.* **2024**, 35, 2419266.
- [9] T. Liu, Y. Zhang, C. Wang, Y. Kang, M. Wang, F. Wu, W. Huang, *Small* **2024**, 20, 2308378.
- [10] X. Dai, Y. Du, J. Yang, D. Wang, J. Gu, Y. Li, S. Wang, B. B. Xu, J. Kong, *Compos. Sci. Technol.* **2019**, 174, 27.
- [11] H. Zhang, Y. Guo, Y. Zhao, Q. Zhu, M. He, H. Guo, X. Shi, K. Ruan, J. Kong, J. Gu, *Angew. Chem., Int. Ed.* **2025**, 64, 202500173.
- [12] H. Ouyang, X. You, Y. Yang, M. Ren, Q. Zhang, R. Deng, X. Zhang, J. Yang, S. Dong, *J. Mater. Sci. Technol.* **2025**, 214, 1.
- [13] W. Kang, Y. Shen, T. Yang, Z. Zhao, Y. Gou, *Adv. Funct. Mater.* **2024**, 35, 2415432.
- [14] M. Niu, H. Wang, L. Su, Z. Cai, D. Lu, H. Gao, L. Xu, K. Peng, L. Zhuang, W. Fu, *J. Am. Ceram. Soc.* **2023**, 106, 3078.
- [15] Y. Guo, L. Zhang, K. Ruan, Y. Mu, M. He, J. Gu, *Polymer* **2025**, 323, 128189.
- [16] G. Li, M. Zhu, W. Gong, R. Du, A. Eychmüller, T. Li, W. Lv, X. Zhang, *Adv. Funct. Mater.* **2019**, 29, 1900188.
- [17] X. Zhang, F. Wang, L. Dou, X. Cheng, Y. Si, J. Yu, B. Ding, *ACS Nano* **2020**, 14, 15616.
- [18] Z. Cai, L. Su, M. Niu, L. Wang, Z. Ni, H. Wang, K. Peng, L. Zhuang, *Adv. Mater. Interfaces* **2022**, 9, 2201553.
- [19] H. Gu, L. Tian, Q. Zhang, X. You, M. Wang, S. Dong, J. Yang, *Small* **2024**, 20, 2402423.
- [20] Z. Wang, Z. Li, B. Li, A. Shi, L. Zhang, Y. Zhu, F. Ye, S. Yu, *Adv. Mater.* **2024**, 36, 2412605.
- [21] C. Guo, S. Shao, X. Zhang, Y. Tang, L. Wang, J. Liu, L. Wu, K. Bi, F. Wang, *Nano Res.* **2024**, 17, 7803.
- [22] S. Shao, C. Guo, H. Wang, S. Wang, T. Zhao, Y. Tang, J. Liu, F. Wang, *Chem. Eng. J.* **2024**, 488, 150918.
- [23] W. Yin, M. Qin, H. Yu, J. Sun, W. Feng, *Adv. Fiber Mater.* **2023**, 5, 1037.
- [24] Q. Wu, J. He, F. Wang, X. Yang, J. Zhu, *Appl. Surf. Sci.* **2020**, 532, 147359.
- [25] J. L. Suter, P. V. Coveney, *Sci. Rep.* **2021**, 11, 22460.
- [26] Y. Zeng, L. Long, J. Yu, Y. Li, Y. Li, W. Zhou, *Compos. Sci. Technol.* **2024**, 250, 110531.
- [27] Y. Cai, Z. Wang, G. Fei, M. Lavorgna, H. Xia, *Adv. Funct. Mater.* **2025**, 2419252.
- [28] K. Zhao, T. Zhang, H. Chang, Y. Yang, P. Xiao, H. Zhang, C. Li, C. S. Tiwary, P. M. Ajayan, Y. Chen, *Sci. Adv.* **2019**, 5, aav2589.
- [29] G. Yang, X. Zhang, R. Wang, X. Liu, J. Zhang, L. Zong, H. Yang, *Mater. Horiz.* **2023**, 10, 1865.
- [30] T. Honma, T. Sato, *J. Supercrit. Fluids* **2020**, 166, 105037.
- [31] H. Chen, X. Liu, S. Zhang, S. Xu, T. Fu, Y. Z. Wang, *Adv. Sci.* **2025**, 12, 2414416.
- [32] M. Hasegawa, R. Tokunaga, K. Hashimoto, J. Ishii, *React. Funct. Polym.* **2019**, 139, 181.
- [33] C. Pu, F. Liu, H. Xu, G. Chen, G. Tian, S. Qi, D. Wu, *Mater. Today Chem.* **2023**, 33, 101679.
- [34] Y. Deng, M. Yang, Y. Wang, M. Zhang, S. Zhou, X. Lu, X. Jian, Y. Chen, *J. Mater. Chem. A* **2024**, 12, 32172.
- [35] X. Liu, W. Ma, T. Yang, Z. Qiu, J. Wang, Y. Li, Y. Wang, Y. Huang, *ACS Nano* **2024**, 18, 10184.
- [36] T. Kato, Y. Yamada, Y. Nishikawa, H. Ishikawa, S. Sato, *Carbon* **2021**, 178, 58.
- [37] M. Yoonessi, Y. Shi, D. A. Scheiman, M. Lebron-Colon, D. M. Tigelaar, R. A. Weiss, M. A. Meador, *ACS Nano* **2012**, 6, 7644.
- [38] Y. Xia, H. Qin, W. Tong, Y. Qi, K. Li, Y. Liu, Z. Xu, Y. Liu, K. Pang, C. Gao, W. Gao, *Adv. Mater.* **2025**, 37, 2417462.
- [39] M. Yang, N. Zhao, Y. Cui, W. Gao, Q. Zhao, C. Gao, H. Bai, T. Xie, *ACS Nano* **2017**, 11, 6817.
- [40] S. Wang, D. Feng, Z. Zhang, X. Liu, K. Ruan, Y. Guo, J. Gu, *Chin. J. Polym. Sci.* **2024**, 42, 897.
- [41] L. Liang, Q. Li, X. Yan, Y. Feng, Y. Wang, H.-B. Zhang, X. Zhou, C. Liu, C. Shen, X. Xie, *ACS Nano* **2021**, 15, 6622.
- [42] W. Huang, M. Song, S. Wang, B. Wang, J. Ma, T. Liu, Y. Zhang, Y. Kang, R. Che, *Adv. Mater.* **2024**, 36, 2403322.
- [43] S. Shao, S. Xing, K. Bi, T. Zhao, H. Wang, Y. Tang, J. Liu, F. Wang, *Chem. Eng. J.* **2024**, 494, 152976.
- [44] Y. Tang, S. Shao, C. Guo, K. Bi, H. Wang, T. Zhao, J. Liu, F. Wang, *Carbon* **2024**, 228, 119314.
- [45] G. Li, S. Ma, Z. Li, Y. Zhang, Y. Cao, Y. Huang, *Adv. Funct. Mater.* **2023**, 33, 2210578.
- [46] X. Huang, J. Wei, Y. Zhang, B. Qian, Q. Jia, J. Liu, X. Zhao, G. Shao, *Nano-Micro Lett.* **2022**, 14, 107.
- [47] H. Tian, J. Lin, J. Liu, L. Li, B. Li, S. Zheng, W. Liu, C. Liu, Z. Zeng, N. Wu, *ACS Appl. Mater. Interfaces* **2024**, 16, 61484.
- [48] J. Ding, R. Shi, C. Gong, C. Wang, Y. Guo, T. Chen, Y. Zhang, H. Cong, C. Shi, F. He, *Adv. Funct. Mater.* **2023**, 33, 2305463.

- [49] D. Lei, C. Liu, C. Dong, S. Wang, P. Zhang, Y. Li, J. Liu, Y. Dong, C. Zhou, *ACS Appl. Nano Mater* **2024**, 7, 230.
- [50] S. Li, Y. Sun, F. Meng, X. Jiang, H. Yu, *Chem. Eng. J.* **2024**, 498, 155405.
- [51] R. Shu, L. Nie, Z. Zhao, X. Yang, *J. Mater. Sci. Technol.* **2024**, 175, 115.
- [52] Y. Yang, Z. Xiu, F. Pan, H. Liang, H. Jiang, H. Guo, X. Wang, L. Li, B. Yuan, W. Lu, *Adv. Funct. Mater.* **2024**, 2406133.
- [53] J. Lin, J. Qiao, H. Tian, L. Li, W. Liu, L. Wu, J. Liu, Z. Zeng, *Adv Compos. Hybrid Mater.* **2023**, 6, 177.
- [54] C. Yu, J. Guo, S. Lv, X. Jiang, *Chem. Eng. J.* **2023**, 468, 143850.
- [55] Y. Wu, Y. Zhao, M. Zhou, S. Tan, R. Peymanfar, B. Aslibeiki, G. Ji, *Nano-Micro Lett.* **2022**, 14, 171.
- [56] Y. Zhang, J. Wang, Q. Wu, T. Shan, S. Bai, D. Lan, B. Zhang, Y. Liu, X. Su, *J. Colloid Interface Sci.* **2025**, 678, 648.
- [57] Y. Guo, Y. Duan, X. Liu, J. Tian, N. Wen, Z. Fan, L. Pan, *Carbon* **2024**, 230, 119591.
- [58] C. Liu, N. Wu, F. Pan, X. Zhang, Z. Wang, L. Wu, J. Lin, W. Liu, J. Liu, Z. Zeng, *Compos. B-Eng.* **2024**, 287, 111835.
- [59] W. Wang, Y. Wang, Z. Lu, R. Cheng, H. Zheng, *Carbon* **2023**, 203, 397.
- [60] J. Yue, Y. Feng, M. Qin, W. Feng, *Nano Res.* **2024**, 17, 883.
- [61] B. Wang, H. Zhang, Q. He, H. Yu, M. Qin, W. Feng, *Chin. J. Polym. Sci.* **2024**, 42, 1002.
- [62] M. Wu, Z. Shao, N. Zhao, R. Zhang, G. Yuan, L. Tian, Z. Zhang, W. Gao, H. Bai, *Science* **2023**, 382, 1379.